REGULAR PAPER

Microstructure and Mechanical Characteristics of Dissimilar TIG Welded 9% Cr Heat-Resistant Steels Joints

Ting Li[1] · Xinjian Yuan[1] · Rui Li[1] · Jiankun Xiong[2] · Shiwei Tao[1] · Kanglong Wu[1]

Abstract

Dissimilar 9% Cr heat-resistant steels (G115 and CB2) with good creep properties for ultra-supercritical steam turbines were butt-joined by tungsten inert gas welding. The microstructure of welded metal (WM) was quenched martensite without carbide precipitates and lath packets existed inside prior austenite grains (PAGs), which leaded to higher hardness of WM. Partially melted zone at G115 side was composed of untempered martensite within equiaxed PAGs. The lowest hardness occurred in both G115 and CB2 steels which was attributed to tempered martensite with many $M_{23}C_6$ precipitates. The heat-affected zone consisted of three sub-grains and their microstructure was detailly analyzed in current work. As current increased from 130 to 150 A, both the tensile strength at room temperature and 650 ℃ increased while strength had no obvious change with further increasing current. The values of 673 MPa and 309 MPa corresponded to the tensile stress with 150 A at room temperature and 650 ℃, respectively. The fracture mode of joints at room temperature was cleavage and ductile failure at 130 and 150 A, respectively. The high-temperature fracture surface at 150 A was composed of deep and fine dimples.

Keywords Heat-resistant steel · Tungsten inert gas welding · Microstructure · Mechanical characteristics · Dissimilar joint

1 Introduction

To achieve the goal of conserving resources and protecting the environment, it is essential to improve thermal efficiency of coal-fired power plants by enhancing steam temperature

✉ Xinjian Yuan
xinjianyuan@yahoo.com; xinjianyuan@cqu.edu.cn

✉ Jiankun Xiong
xiongkai2010@163.com

Ting Li
1985438821@qq.com

Rui Li
1058298572@qq.com

Shiwei Tao
1169953586@qq.com

Kanglong Wu
1430465838@qq.com

[1] College of Materials Science and Engineering, Chongqing University, No. 174, Shazheng Street, Shapingba District, Chongqing 400044, People's Republic of China

[2] Manufacturing Technology Department, Dongfang Turbine Co., Ltd, No. 666, Jinshajiangxi Road, Deyang 618000, People's Republic of China

and pressure [1–3]. This challenge closely depends on the heat-resistant steels used in ultra-supercritical (USC) steam turbines. Hence more attention should be put on the heat-resistant metals applied in USC power plants [4].

The 9% Cr heat-resistant steels are extensively used in elevated temperature components for USC power plants, which is based on their martensitic microstructure, excellent mechanical properties at high temperatures and welding characteristics [5, 6]. Traditional martensitic heat-resistant steels such as T/P91 and T/P92 are usually used in USC power plants at 600 ℃, but the martensitic microstructure is not stable for steam temperatures higher than 600 °C [5, 7]. Tabuchi et al. [8] reported that the modified 9Cr-1Mo steel was widely fabricated in power plants at around 625 ℃. The 9Cr1Mo1CoNiVNbNB (CB2) steel was designed by adding Co and B to modify 9Cr-1Mo martensitic steel, which had excellent creep properties and oxidation resistance at elevated temperatures [9]. Because the addition of B element could improve the stability of $M_{23}C_6$ precipitates and retard their coarsening. Yan et al. [10] introduced that a novel 9Cr3W3CoCuVNbBN (G115) steel was a creep-ductile material and could be candidate material for use in USC power plants with temperatures up to 650 °C. Compared traditional martensitic steels, Mo has been replaced by W

element and the addition of B and Cu could further improve precipitation strengthening [11].

Welding of 9% Cr heat-resistance steels plays an important role in power plant construction. Manugula et al. [12] obtained good welded joints of 9Cr-1.5W steel by electron beam welding. Submerged arc welding was utilized to join dissimilar 9Cr-2Co-1Mo and 2Cr-1Mo steels with 2Cr-1Mo steel as filler metal [13, 14]. Zhang et al. [15] studied the effect of microstructure on mechanical characteristics of welds and stir zones of 9Cr-1.5W steel friction stir welded joints. The $M_{23}C_6$ precipitates in stir zone almost or even completely dissolved during friction stir welding, while MX carbonitrides and M_3C particles were main dispersed strengthening phases. Considering high cost and fast wear of the stir-welding head, tungsten inert gas (TIG) or gas tungsten arc welding is more suitable for joining 9% Cr heat-resistant steels [16]. Pandey et al. [12] discussed the microstructure and mechanical characteristics of the 9Cr-2W steel welded joints by TIG welding. Previous literature [17] also reported that 9Cr-1Mo steel was successfully butt-joined by activating flux TIG (A-TIG) welding with multicomponent flux. Compared with the conventional TIG weldments, joint penetration had an increase of 200% and 300% with CeO_2 and MoO_3 based flux, respectively. Tensile properties of weldments were almost same, while the impact toughness was much less than that of the base metal. Arivazhagan et al. [18] studied the differences on the microstructure and toughness of 9Cr-1Mo steel welded joints by traditional gas tungsten arc welding and A-TIG welding. Laser-TIG hybrid welding joined two 9Cr-1.5W steel plates with thickness of 3 mm [19].

MARBN (9Cr3W3Co0.2V0.05Nb) steels [20] were developed for USC power plants by Japan and they were much similar to G115 in terms of chemical composition. Main welding method for these steels was gas tungsten arc welding with Inconel-type filler as welded metal [8, 20]. The application of Ni-base wire was restricted by high cost and different physical properties between Ni-base wire and steel [21, 22]. In contrast, iron-base wire has been widely used to join heat resistant steels in coal-fired power plants. But few literatures studied TIG-welding of dissimilar G115 and CB2 steels with iron-base filler metal. The filler weir used in current work was designed for G115 and its chemical composition was much similar to G115 steel. This work investigated the effect of welding current on microstructure and tensile properties of G115/CB2 welded joints at room temperature

and at an operating temperature of 650 ℃. The fracture morphology and location were analyzed by scanning electron microscopy (SEM) and optical microscope (OM). Meanwhile the microstructure of joints was detailly observed by SEM, electron back-scattered diffraction (EBSD), and transmission electron microscope (TEM).

1.1 Materials and Experiment

In current experiment, G115 and CB2 steels were used as base metals. TIG welding was applied to butt-join G115 and CB2 steels with filler wire, and its diameter was 2.4 mm. Their chemical composition was listed in Table 1.

Prior welding, G115 and CB2 steels were processed into specimens with the size of 80 mm × 70 mm × 2 mm (based on Enterprise standard), and the oxides on the welded regions were ground via abrasive paper. A TIG welding machine (YC-300WP5HGN, PWST, China) was used to weld G115 and CB2 plates, and its schematic diagram was shown in Fig. 1a. During welding, argon (Ar) was utilized to protect the weld pool from oxidation. The main purpose of 2 mm wide gap between two plates was to guarantee high penetration of welded metal (WM), which could realize single-side welding with double-sided forming. The TIG welding parameters were exhibited in Table 2, and the value of welding current was 110, 130, 150, 170 and 190 A, respectively. The lower welding current of 90 A was not included in parameter range because there was no effective connection between G115 and CB2 at this current. Without significant change in performance of welded joints, from the perspective of energy conservation and electrode loss, the welding of higher current has not been carried out.

After welding, cross-sectional samples were cut from welded joints by wire cutting and the size of samples was 35 mm × 5 mm. Then samples were ground with water abrasive paper and polished with 2.5 μm diamond paste. Cross-sections were chemically etched (5 g $FeCl_3$ +15 ml HCl + 80 ml H_2O) for 10 s to achieve OM and SEM observation. The EBSD was used to investigate microstructure of welded joints, and the morphology and composition of precipitates were analyzed by TEM. The size and preparation of EBSD sample were similar to metallographic samples, but it

Table 1 Chemical composition of base metals and filler wire (wt.%)

Elements	C	Cr	W	Co	Mo	Cu	Mn	Si	Ni	V	Nb	N	B	Fe
CB2	0.11	9.18	–	0.98	1.47	–	0.69	0.3	0.33	0.2	0.06	0.02	0.009	Bal
G115	0.08	8.8	2.84	3.0	–	1.0	0.5	0.3	–	0.2	0.06	0.008	0.014	Bal
Filler wire	0.088	8.95	2.8	3.01	–	0.94	0.35	0.07	–	0.22	0.008	0.0096	0.009	Bal

Fig. 1 Schematic illustrations of **a** TIG welding process, **b** tensile sample at room temperature, **c** tensile sample at 650 ℃
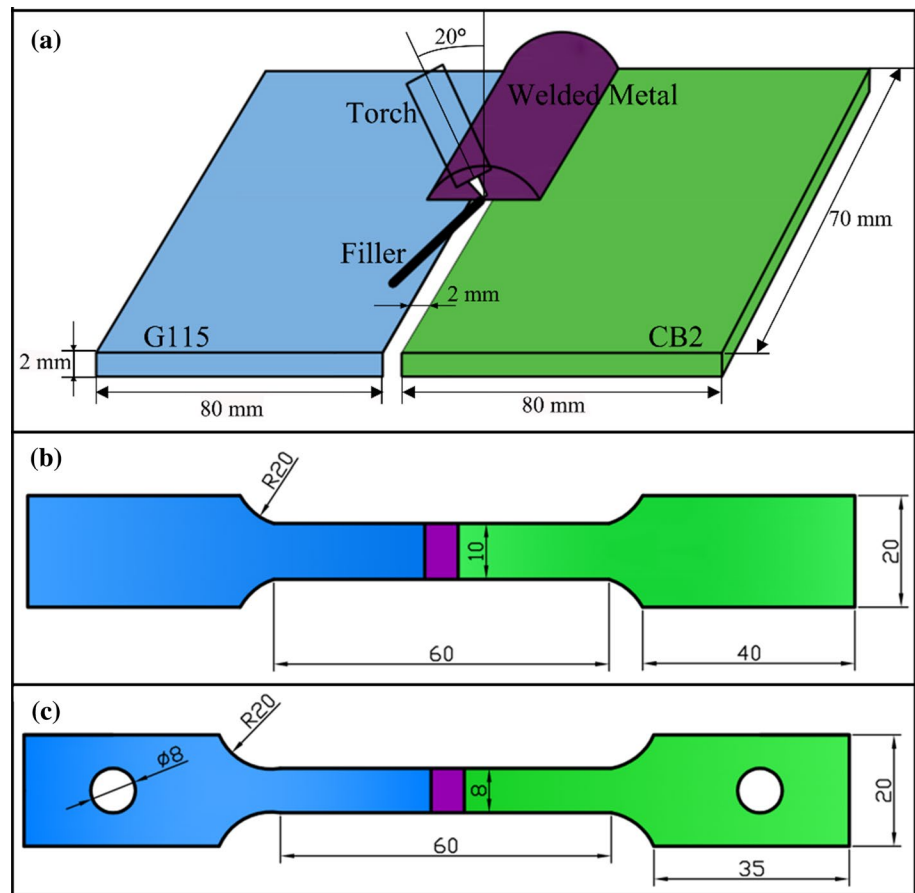

Table 2 TIG welding process parameters

Welding parameters	Value
Welding current (A)	110–190
Welding speed v (m/min)	0.15
Welding arc length L (mm)	1
Wire feed speed v_1 (m/min)	0.5
Flowrate of shielding gas (Ar) R (l/min)	10

was corroded by electrolytic polishing (6%HClO$_4$ + 94%C$_2$H$_5$OH) with voltage of 20 V and holding time of 10 s. EBSD images were obtained under the conditions of 12 A current, 15 V voltage, 0.5 μm step size and 400× magnification, and the raw indexing percentage was about 75–90%. The TEM sample was obtained by twin-jet electropolish (5%HClO$_4$ + 95%C$_2$H$_5$OH), and the voltage and temperature were 45 V and -35 ℃, respectively. Mechanical characteristics involved Vickers microhardness, tensile strength at room temperature and 650 ℃. Microhardness measurement was implemented with a Vickers load (MH3N) of 4.9 N and a dwelling time of 5 s. The tensile samples were cut from weldments, then superfluous welded metal

was ground by grinding machine, thereby getting reliable tensile strength. The dimensions of the room temperature tensile test sample matched with the GB/T228-2002 standard, as presented in Fig. 1b. Tensile tests at room temperature were carried out by an electronic tensile test machine (AG-X, SHIMADZU, Japan), where the loading rate was 1 mm/min. Tensile tests at 650 ℃ were performed in an elevated temperature chamber with a loading speed of 1 mm/min, and its schematic figure was illustrated in Fig. 1c. Fracture location and morphology were analyzed by OM and SEM, respectively.

2 Results and Discussion

2.1 Macro Characteristics of Welded Joints

Figure 2 illustrates the effect of welding current on macro-morphology of TIG-welded joints. Figure 2a–d depict the appearance of the top surface of joints, and their welding current was 110, 130 150 and 170 A,
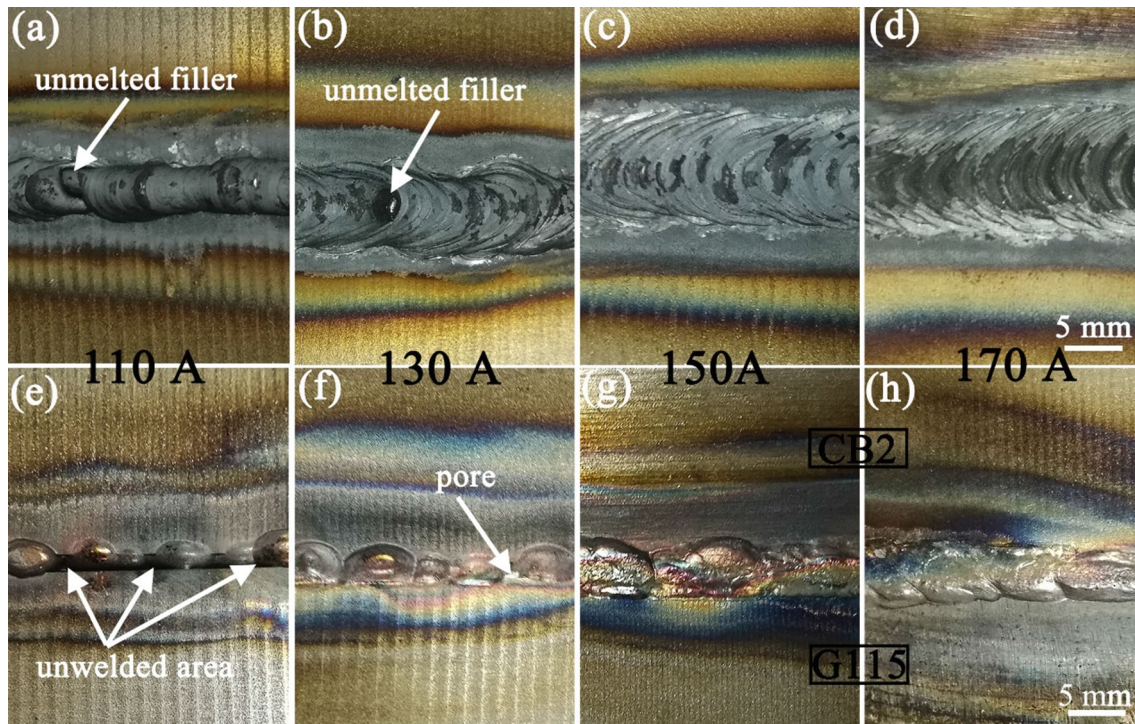
Fig. 2 Macro-morphology of welded joints: **a–d** were top surfaces at 110, 130, 150 and 170 A, respectively, **e–h** were their root surfaces, respectively

respectively. Figure 2e-h correspond to the root surface of their joints, respectively. Owing to fixed welding speed, the heat input at 110 and 130 A was insufficient to melt all filler wire, leading to un-melted filler left in WM, as shown in Fig. 2a and b, meanwhile the higher and narrower WM was observed at lower current. In Fig. 2e and f, pores were found on the root surface and the welded area was very small at 110 A, indicating that full penetration was not realized at 110 and 130 A. The main reason was that the spreading of liquid welded metal was partially limited by un-melted filler. When current increased to 150 and 170 A, more heat input promoted the formation of WM and the WM was

continuous on the top and root surfaces, achieving full penetration throughout the weld length, as exhibited in Fig. 2c, d, g, f.

Figure 3a and b are cross-sectional macrostructure images with welding current of 130 and 150 A, respectively. There were soft ferrite patches in WM near CB2, as arrows marked in Fig. 3a. Figure 4a and b are magnified OM images of ferrite marked in Fig. 3a, which was consistent with this literature [12]. It could be obviously noticed that the martensite of WM seems to be coarser at 150 A, which was attributed to heat input. In Fig. 3b, the profile of WM on top and root sides was more symmetrical than that of Fig. 3a, and

Fig. 3 Cross-sectional macrostructure images of welded joints: **a** 130 A, **b** 150 A
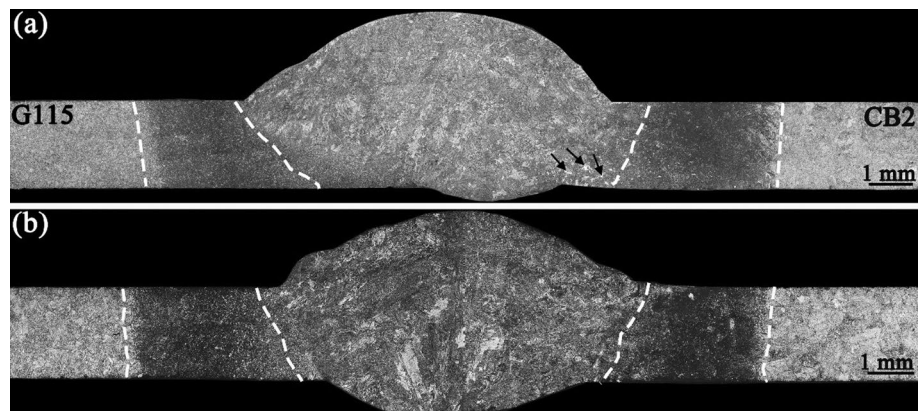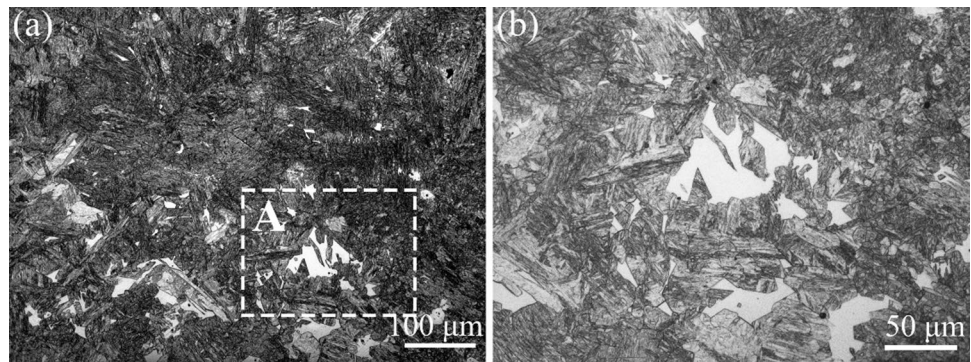
Fig. 4 **a** OM image of WS near CB2 at 130 A, **b** magnified image of area A

the WM of Fig. 3a on the top side was higher. The width of HAZ was approximately 3 mm in both sides of G115 and CB2, and large HAZ was associated with high heat input and thin plates.

2.2 Microstructure of Welded Joints

Figures 5 and show the microstructure of WM with different welding current of 130 and 150 A, respectively. In both WM, quenched lath martensite was noticed inside the prior austenite grains (PAGs) (marked by white dotted line) and a large number of laths formed lath packets (presented by orange dotted line). There were some cavities in WM formed during the solidification process of weld pool, as shown in Fig. 5b, which might influence the mechanical properties of joints. Figure 6b is the magnified SEM image of WM, and the width of lath martensite varied from 0.5 μm to 1.5 μm. The EBSD of Fig. 6c illustrates the lath characteristic of martensite and the orientation of martensite in packets was basically consistent. Figure 7 gives TEM result of WM, Fig. 7a and b illustrate that the microstructure of WM was lath martensite, and some dislocations distributed on the

laths at 150 A. No precipitate was found in WM owing to high cooling rate. The martensite was body-centered cubic structure, which was confirmed by Fig. 7c.

Figure 8a shows the OM of joint transition zone at G115 side at 150 A, and it consists of WM, partially melting zone (PMZ), HAZ and base metal (BM). During TIG welding process, the peak temperature of welding thermal cycle decreased from WM to BM, thus the HAZ was divided into three sub-zones: coarse grain heat affected zone (CGHAZ), fine grain heat affected zone (FGHAZ) and inter critical heat affected zone (ICHAZ). Figure 8b-e show the EBSD of CGHAZ, FGHAZ, ICHAZ and BM, respectively, corresponding to region A, B, C and D in Fig. 8a.

The microstructure of CGHAZ and FGHAZ was untempered martensite in PAGs [6]. Average grain size of CGHAZ was 50 μm, estimated from Fig. 7b. During TIG welding, the temperature of CGHAZ could far exceed Ac_3, promoting prior austenite grain growth, as illustrated by Pandey et al. [23]. The temperature of FGHAZ was just above Ac_3, and the dwelling time was short due to faster cooling rate. Finer grains (average grain size of 10 μm) are observed in Fig. 8c. Figure 8d presents the microstructure of ICHAZ, which was composed of untempered and tempered martensite [24]. The temperature of ICHAZ was between Ac_1 and Ac_3,
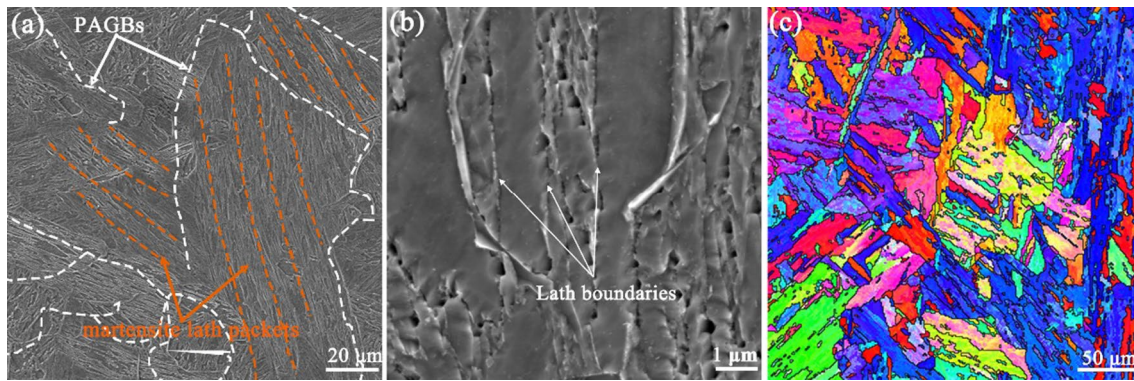
Fig. 5 SEM images of WM at 130 A
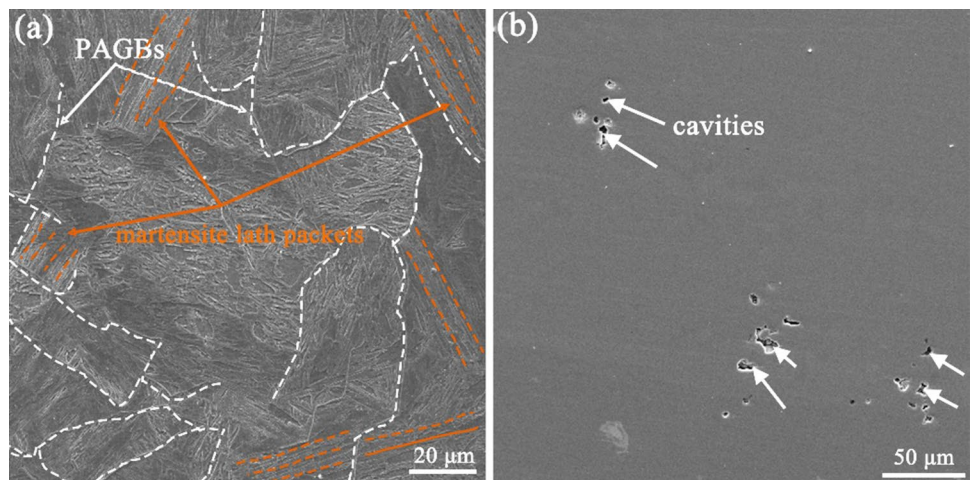
Fig. 6 Microstructure of WM at 150 A: **a** SEM image, **b** magnified SEM image, **c** EBSD image
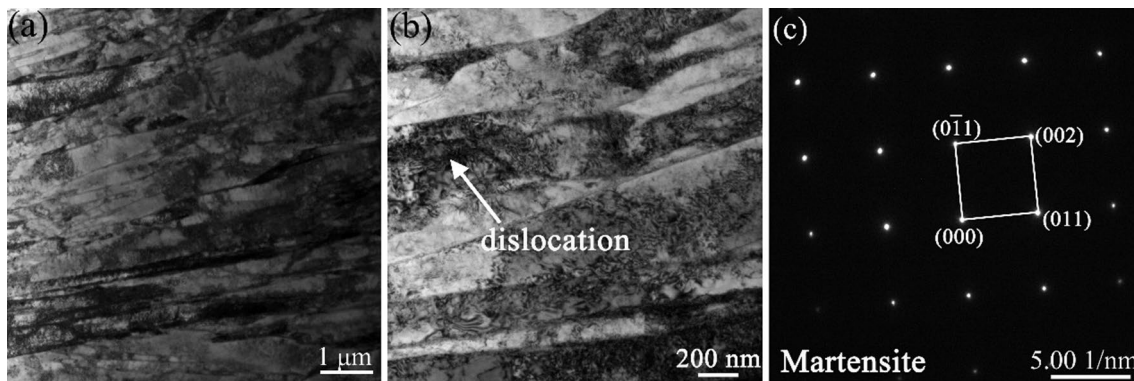

Fig. 7 TEM analysis of WM: **a** and **b** morphologies of martensite, **c** diffraction pattern of matrix

and partial tempered martensite transformed into austenite, subsequently forming quenched martensite by air cooling process. Fig. 8(e) presents that the microstructure of BM was tempered martensite blocks. Figure 9 gives the TEM result of G115 steel, and Fig. 9a and b prove that tempered martensite inside PAGs was main structure of G115 steel and some dislocations and dislocation tangles distributed on laths. From Fig. 9c, some precipitates with width of 200 nm exist along prior austenite grain boundaries (PAGBs). Figure 9d presents the chemical composition of precipitates marked in Fig. 9c, and their composition seems to be similar, namely W-enriched $M_{23}C_6$ (M: Fe or Cr) phase.

Figure 10a is EBSD image of WM and PMZ, revealing that PMZ lied along WM boundary in welded joint at 150 A. Combined with Fig. 10b of SEM image, PMZ was composed of equiaxed PAGs with average diameter of 15 µm and its microstructure was quenched martensite. During welding, the temperature of WM exceeded the liquidus temperature of the alloy, the temperature of HAZ was higher than a critical value Ac_1 but lower than the solidus temperature of the alloy, and PMZ was a region in which the experienced temperature was between solidus and liquidus of the BM. Therefore, the PMZ consisted of

molten metal and solids, and this region was closed to HAZ, which would promote heterogeneous nucleation and increased the rate of nucleation. In addition, fast cooling rate also restricted the grain growth.

Figure 11a reveals that the transition joint at CB2 side consisted of WM, HAZ with three sub-regions and BM at 150 A. Figure 11b–e correspond to region A, B, C and D of Fig. 11a, respectively. According to Fig. 11b, CGHAZ was composed of coarse martensite blocks, while FGHAZ was comprised of untempered martensite within equiaxed PAGs. Compared with HAZ of G115 steel, the grain size of CGHAZ and FGHAZ at CB2 steel seems to be larger. The microstructure of ICHAZ at CB2 side was untempered and tempered martensite, which was similar to ICHAZ at G115 side. Coarse tempered-martensite blocks are presented in Fig. 11e. Figure 12 is TEM images of CB2 steel, and Fig. 12a and b illustrate that the microstructure of CB2 steel was martensite-dominated structure. Some precipitates distributed along martensite-lath border and inside laths. Figure 12c is diffraction pattern of precipitate marked in Fig. 12b, demonstrating that the precipitate was $M_{23}C_6$(M: Fe or Cr) particle with face-centered cubic structure.

Fig. 8 **a** OM of joint transition zone at G115 side, EBSD images of **a**) CGHAZ, **b** FGHAZ, **c** ICHAZ and **d** BM
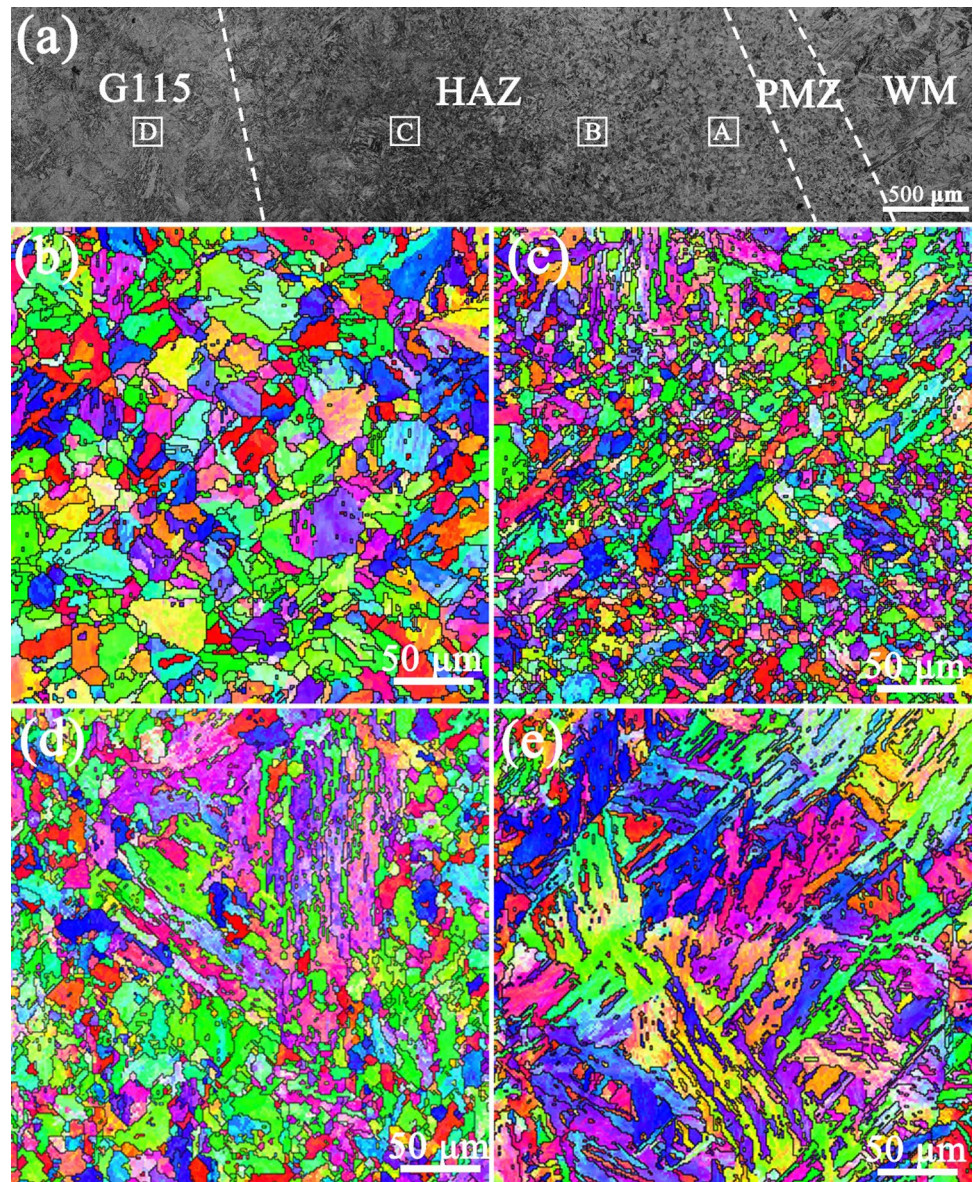
2.3 Microhardness

Figure 13 gives microhardness profiles along the transverse direction of a half thickness of base metals from G115 across WM to CB2 steel, and hardness point was measured at an interval of 0.25 mm. Average hardness of G115 and CB2 steel was about 249 HV and 254 HV, respectively. The specific value of 396 HV and 449 HV corresponded to the average hardness of WM at 130 and 150 A, respectively. Compared with BMs, higher hardness was occurred in WM, which could be attributed to quenched martensite with high carbon content in WM.

The width of PMZ at G115 side was approximately 300 μm, hence it was unnecessary to detailly analyze its hardness.

For the HAZ, the variation of hardness was basically identical at G115 and CB2 side, as shown in Fig. 13. The highest hardness was occurred in CGHAZ closed to WM, and with increased distance from WM, the microhardness of HAZ gradually decreased. Liu et al. [13] reported that the peak temperature become higher, resulting in decreasing carbide particles and the increasing carbon content of martensite. The peak temperature of CGHAZ was higher than that of FGHAZ, and more precipitates dissolved into the matrix, which resulted in higher hardness occurred in CGHAZ [25, 26]. The microhardness of ICHAZ was lower than other HAZ because the microstructure of this region was mixture of tempered and quenched martensite.
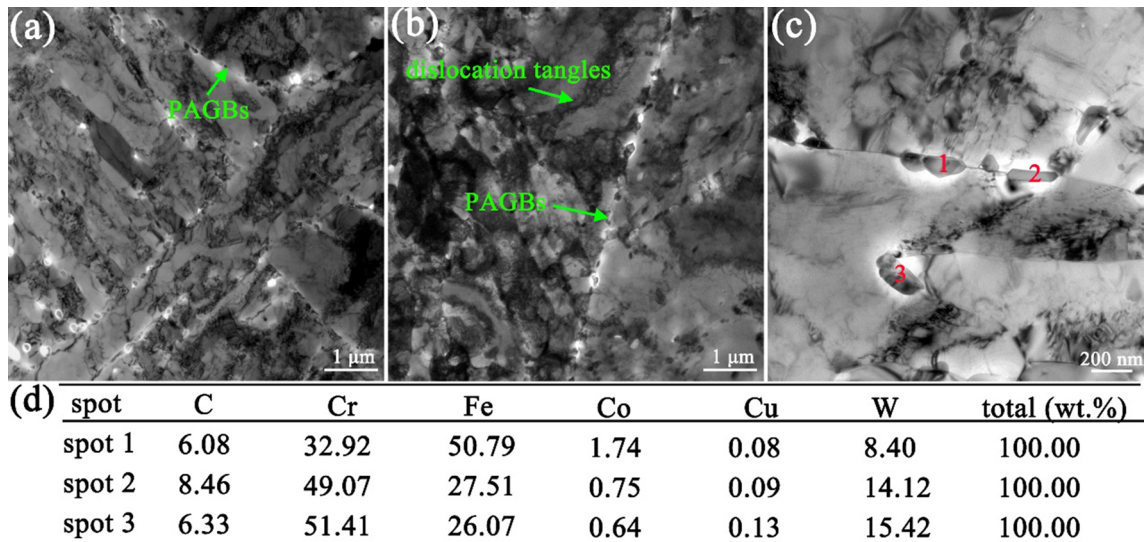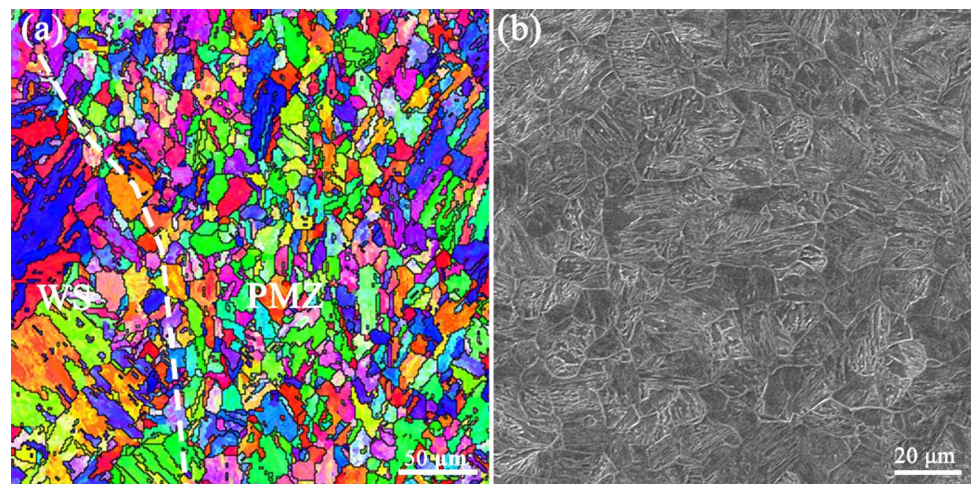
spot	C	Cr	Fe	Co	Cu	W	total (wt.%)
spot 1	6.08	32.92	50.79	1.74	0.08	8.40	100.00
spot 2	8.46	49.07	27.51	0.75	0.09	14.12	100.00
spot 3	6.33	51.41	26.07	0.64	0.13	15.42	100.00

Fig. 9 TEM results of G115 steel: **a** and **b** microstructural morphology of martensite and PAGBs, **c** and **d** the distribution and chemical composition of precipitates

Fig. 10 **a** EBSD image of WM and PMZ, **b** SEM of PMZ

2.4 Tensile Test

2.4.1 Mechanical Properties

The effect of welding current on tensile strength at room temperature is depicted in Fig. 14. The joint at 110 A had the lowest tensile strength due to very small welded zone, as proved by Fig. 3a and e. With increasing current from 110 to 150 A, the tensile strength gradually increased. The tensile stress at 130 A was lower than that of 150 A because lower heat input made filler incompletely melt and some unwelded pores existed on the root surface of WM, partly deteriorating mechanical properties of joints. Sound joints were obtained with larger current of 150 A, as shown in Figs. 3c and g and its tensile strength was 673 MPa. As welding current exceeded 150 A, the tensile strength basically kept stable and had no obvious change. It could be explained that the failure of these tensile samples occurred in the base metals, not influenced by WM and HAZ.

Figure 15 is macroscopic photo of specimens after the tensile test at 130 A and 150 A, respectively. Figure 16a and b present the longitudinal cross-sectional images of facture at 130 and 150 A, respectively. Figure 17a and b are their SEM images of the fracture morphology, respectively. As shown in Figs. 15 and 16a, the tensile specimen at 130 A failed in WM and there was no tensile deformation at the fracture site. Therefore, brittle fracture was fracture mode of welded joint at 130 A, which was also proved by quasi-cleavage areas in Fig. 17a. As current increased to 150 A, obvious plastic deformation and necking were observed at the fracture location because failure appeared in G115 steel, as shown in Figs. 15 and 16b. Fractograph of Fig. 17b presents a large number of fine dimples on

Fig. 11 **a** OM of joint transition zone at CB2 side, EBSD images of **b** CGHAZ, **c** FGHAZ, **d** ICHAZ and **e** CB2 steel

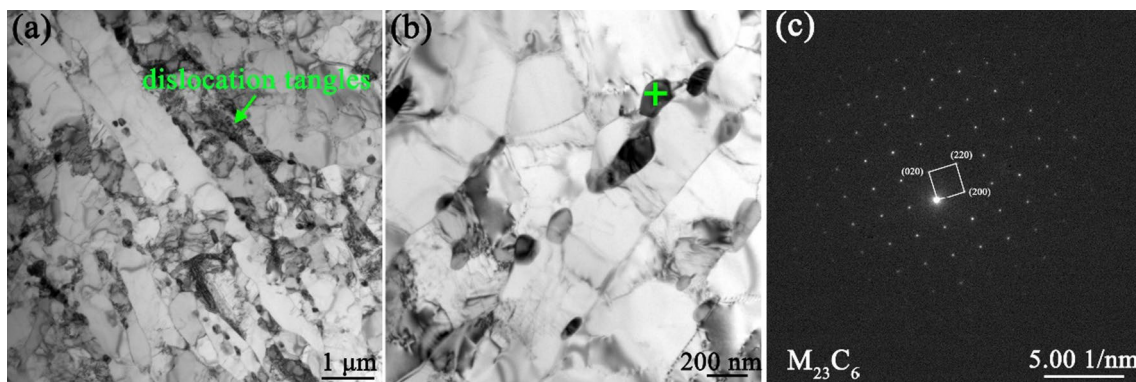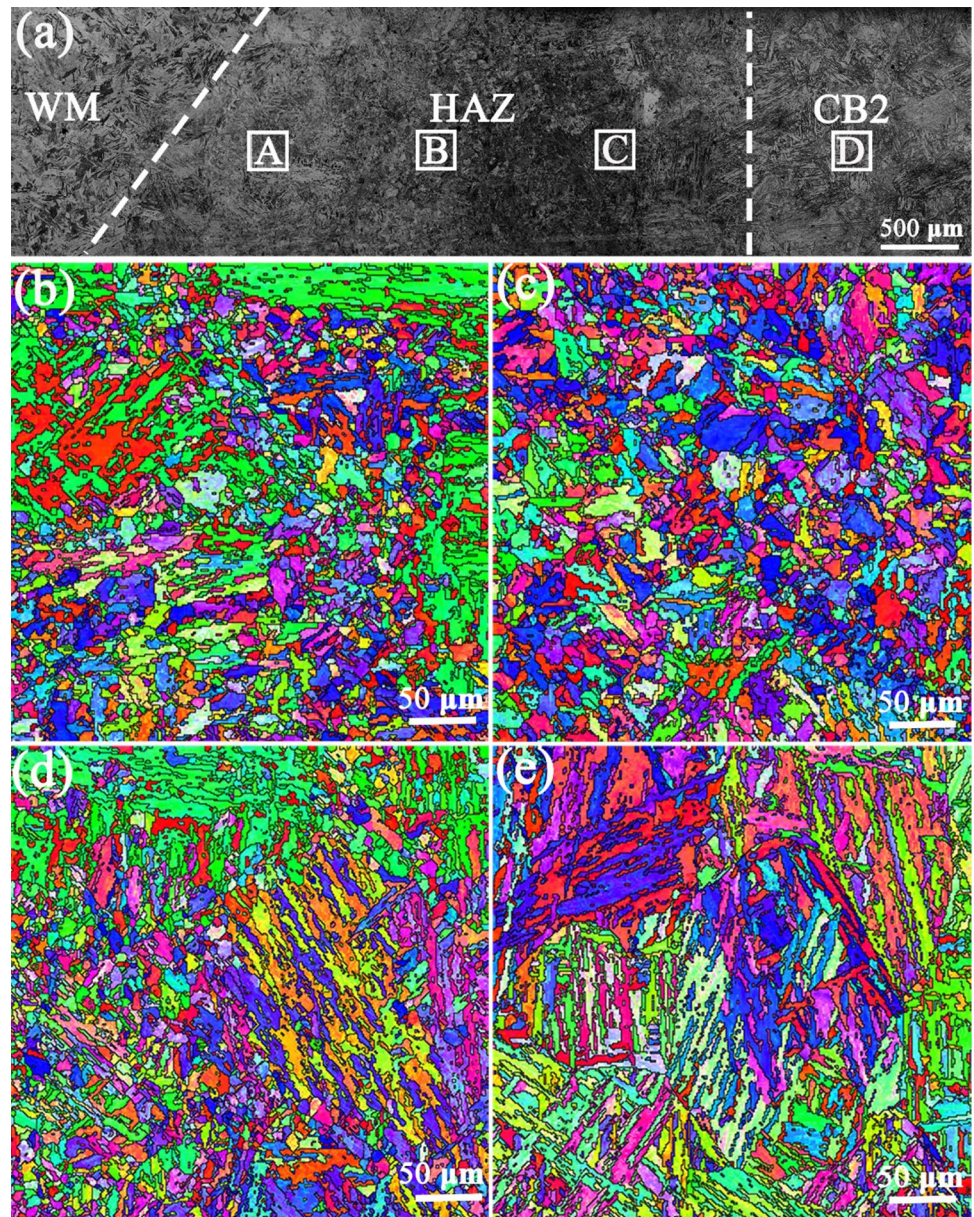**Fig. 12** TEM images of CB2 steel: **a** martensite morphology, **b** precipitate distribution, **c** diffraction pattern of precipitate marked in (**b**)
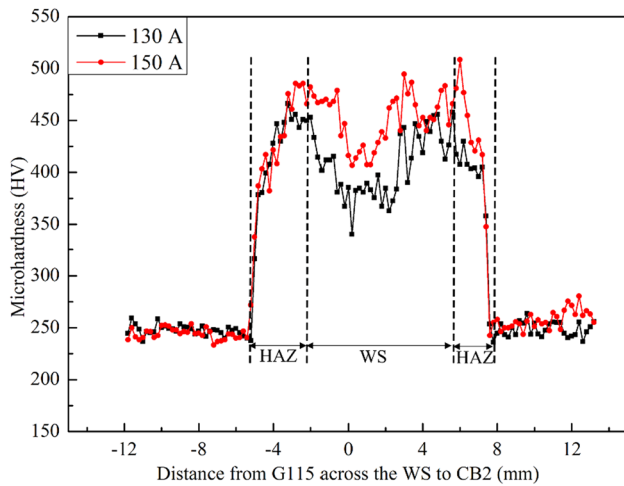
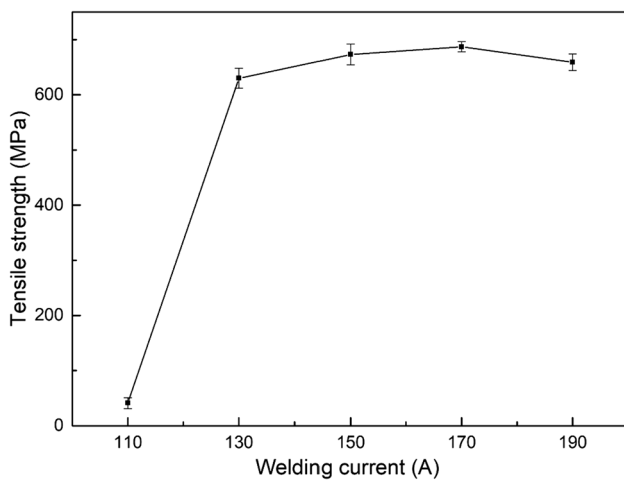**Fig. 13** Microhardness profiles of joints with 130 and 150 A

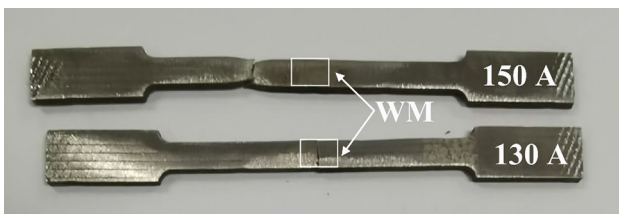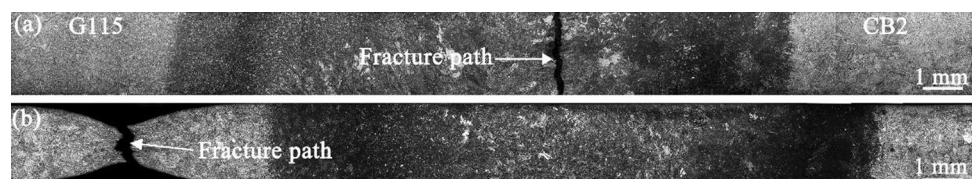**Fig. 14** Tensile strength with different welding current at room temperature

Fig. 15 Macro photo of specimens after the tensile test at 130 A and 150 A

Fig. 16 Longitudinal cross-sectional images of fracture at room temperature: **a** 130 A, **b** 150 A

the fracture surface, which indicates that ductile fracture was the fail mode of welded joints at 150 A.

2.4.2 Elevated-Temperature Behavior

The 9% Cr heat-resistant steels were widely applied in high-temperature conditions, so it was essential to explore the mechanical characteristics of welded joints at an operating temperature of 650 ℃. Figure 18a is the engineering stress–strain curves at 650 ℃ with various welding current. According to Fig. 18a, lower tensile strength and elongation of joint were observed at 130 A, while elevated-temperature strength at 150, 170 and 190 A was almost same and higher than that of 130 A. Based on energy conservation and emission reduction, 150 A was suggested as the optimal welding current in this work and its tensile stress at 650 ℃ was 309 MPa. The tensile stress at 650 ℃ was slightly less than half of tensile strength at room temperature. Wang et al. [27] reported that at 650 ℃, fast diffusion could assist dislocation in bypassing nano-sized precipitates by means of climbing. With the decreasing interaction between precipitates and matrix, precipitate strengthening gradually weakened and the tensile strength subsequently decreased. Xiao et al. [28] also reported that this phenomenon might be related to subgrain coarsening and decreasing dislocation density. Figure 18b exhibits SEM picture of fracture morphology at 150 A. Dense inhomogeneous dimples were noticed in Fig. 18b. These deep dimples were formed by microcavities coalescence, but there were fine dimples existed between deep dimples, which could ascribe to precipitates located in these regions [29].

3 Conclusion

G115 and CB2 steels for ultra-supercritical power plants were successfully joined by TIG welding. Major conclusions were listed as follows:

1. The microstructure of WM at 130 and 150 A was quenched lath martensite inside PAGs, but the microstructure at 130 A was smaller and some cavities were found in its WM, which could influence tensile properties. The microstructure of CB2 and G115 was composed of tempered martensite with $M_{23}C_6$ precipitates.
2. For HAZ at both sides, the peak temperature decreased with increasing distance from WM,

Fig. 17 SEM images of the fracture surface at room temperature: **a** 130 A, **b** 150 A
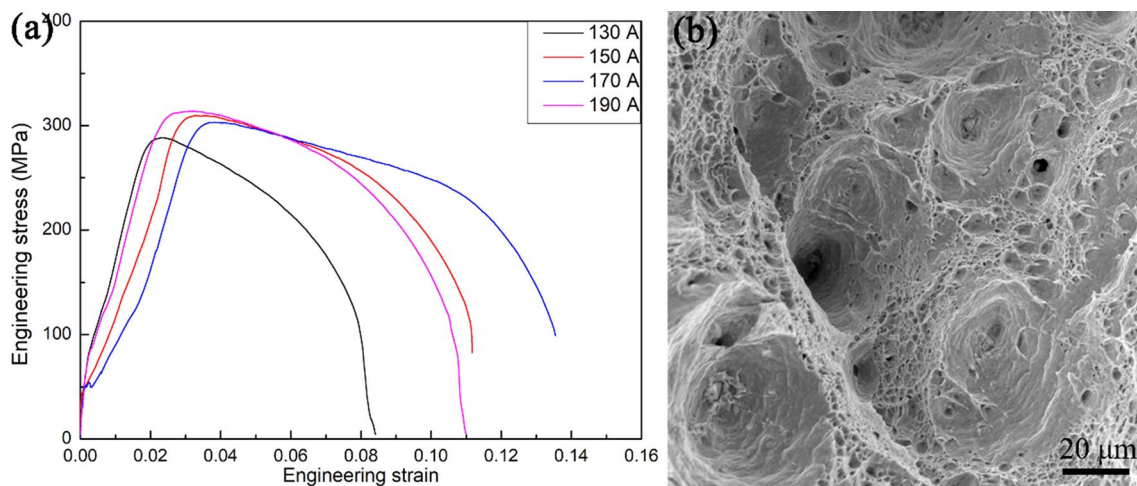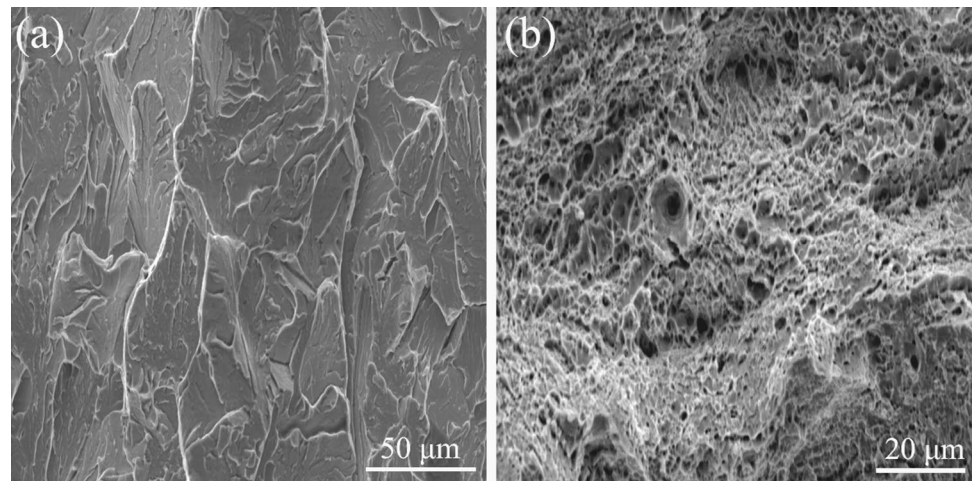

Fig. 18 (a) Engineering stress–strain curves at 650 ℃ with various welding current, (b) fracture morphology at 150A

thus the size of PAGs at CGHAZ was larger than that of FGHAZ. The microstructure of CGHAZ and FGHAZ was untempered martensite, while the ICHAZ was composed of quenched and tempered martensite.

3. The microhardness of WM was higher than that of HAZ and BM, and the hardness of two base metals was about 250 HV. The variation of hardness at both sides was basically similar, and the hardness value of HAZ gradually decreased with increasing distance from WM.

4. The tensile strength at room temperature gradually increased with increasing welding current, and the stress at 150 A was 673 MPa. As current exceeded 150 A, the tensile stress basically kept unchanged. This phenomenon also occurred at 650 ℃, and the tensile strength at 150 A was 309 MPa.

References

1. Xiao, B., Xu, L., Zhao, L., Jing, H., Han, Y., & Song, K. (2018). Transient creep behavior of a novel tempered martensite ferritic steel G115. *Materials Science and Engineering: A, 716*, 284–295.

2. Zhang, X. Z., Wu, X. J., Liu, R., Liu, J., & Yao, M. X. (2017). Deformation-mechanism-based modeling of creep behavior of modified 9Cr-lMo steel. *Materials Science and Engineering: A, 689*, 345–352.

3. Saini, N., Pandey, C., & Mahapatra, M. M. (2017). Effect of normalizing temperature on fracture characteristic of tensile and impact tested creep strength-enhanced Ferritic P92 steel. *Journal of Materials Engineering and Performance, 26*(11), 5414–5424.

4. Pandey, C., & Mahapatra, M. M. (2016). Effect of heat treatment on microstructure and hot impact toughness of various zones of P91 welded pipes. *Journal of Materials Engineering and Performance, 25*(6), 2195–2210.

5. Wang, S. S., Peng, D. L., Chang, L., & Hui, X. D. (2013). Enhanced mechanical properties induced by refined heat treatment for 9Cr-0.5Mo-1.8W martensitic heat resistant steel. *Materials and Design, 50*, 174–180.

6. Sawada, K., Hara, T., Tabuchi, M., Kimura, K., & Kubushiro, K. (2015). Microstructure characterization of heat affected zone after welding in Mod. 9Cr-1Mo steel. *Materials Characterization, 101*, 106–113.

7. Hald, J. (2017). High-alloyed martensitic steel grades for boilers in ultra-supercritical power plants. In *Materials for Ultra-Supercritical and Advanced Ultra-Supercritical Power Plants* (pp. 77–97).

8. Tabuchi, M., Kondo, M., Watanabe, T., Hongo, H., Yin, F., & Abe, F. (2004). Improvement of type IV cracking resistance of 9Cr heat resisting steel welement by boron. *Acta Metallurgica Sinica, 17*(4), 331–337.

9. Agamennone, R., Blum, W., Gupta, C., & Chakravartty, J. K. (2006). Evolution of microstructure and deformation resistance in creep of tempered martensitic 9–12%Cr–2%W–5%Co steels. *Acta Materialia, 54*(11), 3003–3014.

10. Yan, P., Liu, Z., Bao, H., Weng, Y., & Liu, W. (2013). Effect of microstructural evolution on high-temperature strength of 9Cr-3W-3Co martensitic heat resistant steel under different aging conditions. *Materials Science and Engineering: A, 588*, 22–28.

11. Xiao, B., Xu, L., Zhao, L., Jing, H., Han, Y., & Tang, Z. (2017). Microstructure evolution and fracture mechanism of a novel 9Cr tempered martensite ferritic steel during short-term creep. *Materials Science and Engineering: A, 707*, 466–477.

12. Pandey, C., Mahapatra, M. M., Kumar, P., Thakre, J. G., & Saini, N. (2019). Role of evolving microstructure on the mechanical behaviour of P92 steel welded joint in as-welded and post weld heat treated state. *Journal of Materials Processing Technology, 263*, 241–255.

13. Liu, X., Lu, F., Yang, R., Wang, P., Xu, X., & Huo, X. (2015). Investigation on mechanical properties of 9%Cr/CrMoV dissimilar steels welded joint. *Journal of Materials Engineering and Performance, 24*(4), 1434–1440.

14. Zhang, W. C., Zhu, M. L., Wang, K., & Xuan, F. Z. (2018). Failure mechanisms and design of dissimilar welds of 9%Cr and CrMoV steels up to very high cycle fatigue regime. *International Journal of Fatigue, 113*, 367–376.

15. Zhang, C., Cui, L., Liu, Y., Liu, C., & Li, H. (2018). Microstructures and mechanical properties of friction stir welds on 9% Cr reduced activation ferritic/martensitic steel. *Journal of Materials Science and Technology, 34*(5), 756–766.

16. Kim, K. H., Bang, H. S., Ro, C. S., & Bang, H. S. (2017). Influence of preheating source on mechanical properties and welding residual stress characteristics in ultra thin ferritic stainless steel hybrid friction stir welded joints. *International Journal of Precision Engineering and Manufacturing-Green Technology, 4*(4), 393–400.

17. Vidyarthy, R. S., & Dwivedi, D. K. (2018). Microstructural and mechanical properties assessment of the P91 A-TIG weld joints. *Journal of Manufacturing Processes, 31*, 523–535.

18. Arivazhagan, B., & Vasudevan, M. (2014). A comparative study on the effect of GTAW processes on the microstructure and mechanical properties of P91 steel weld joints. *Journal of Manufacturing Processes, 16*(2), 305–311.

19. Li, X., Chen, J., Hua, P., Chen, K., Kong, W., Chu, H., et al. (2018). Effect of post weld heat treatment on the microstructure and properties of Laser-TIG hybrid welded joints for CLAM steel. *Fusion Engineering and Design, 128*, 175–181.

20. Abe, F., Tabuchi, M., Tsukamoto, S., & Shirane, T. (2010). Microstructure evolution in HAZ and suppression of Type IV fracture in advanced ferritic power plant steels. *International Journal of Pressure Vessels and Piping, 87*(11), 598–604.

21. Singh, T., Dureja, J. S., Dogra, M., & Bhatti, M. S. (2018). Environment friendly machining of Inconel 625 under Nano-Fluid Minimum Quantity Lubrication (NMQL). *International Journal of Precision Engineering and Manufacturing, 19*(11), 1689–1697.

22. Liao, Y. S., Liao, C. H., & Lin, H. M. (2017). Study of oil-water ratio and flow rate of MQL fluid in high speed milling of Inconel 718. *International Journal of Precision Engineering and Manufacturing, 18*(2), 257–262.

23. Pandey, C., Mahapatra, M. M., Kumar, P., Kumar, S., & Sirohi, S. (2019). Effect of post weld heat treatments on microstructure evolution and type IV cracking behavior of the P91 steel welds joint. *Journal of Materials Processing Technology, 266*, 140–154.

24. Wang, Y., Kannan, R., & Li, L. (2016). Characterization of as-welded microstructure of heat-affected zone in modified 9Cr–1Mo–V–Nb steel weldment. *Materials Characterization, 118*, 225–234.

25. Vidyarthy, R. S., Kulkarni, A., & Dwivedi, D. K. (2017). Study of microstructure and mechanical property relationships of A-TIG welded P91–316L dissimilar steel joint. *Materials Science and Engineering: A, 695*, 249–257.

26. Pandey, C., & Mahapatra, M. M. (2016). Effect of Groove Design and Post-Weld Heat Treatment on Microstructure and Mechanical Properties of P91 Steel Weld. *Journal of Materials Engineering and Performance, 25*(7), 2761–2775.

27. Wang, L., Li, M., & Almer, J. (2013). In situ characterization of Grade 92 steel during tensile deformation using concurrent high energy X-ray diffraction and small angle X-ray scattering. *Journal of Nuclear Materials, 440*(1–3), 81–90.

28. Xiao, B., Xu, L., Zhao, L., Jing, H., & Han, Y. (2017). Tensile mechanical properties, constitutive equations, and fracture mechanisms of a novel 9% chromium tempered martensitic steel at elevated temperatures. *Materials Science and Engineering: A, 690*, 104–119.

29. Xiao, B., Xu, L., Zhao, L., Jing, H., Han, Y., & Zhang, Y. (2018). Creep properties, creep deformation behavior, and microstructural evolution of 9Cr-3W-3Co-1CuVNbB martensite ferritic steel. *Materials Science and Engineering: A, 711*, 434–447.

Ting Li received her master's degree in Materials Science and Engineering from Chongqing University in 2020. She presently works as an assistant engineer in the College of Materials Science and Engineering, Chongqing University, China. Her research interests are Material Processing and Welding of Material.

Jiankun Xiong received his PhD degree in Department of Mechanical Engineering from Tsinghua University, China, in 2019. He is currently a senior researcher and the director of Manufacturing Technology Department in Dongfang Turbine Co., Ltd. His current research interests include production technology planning, Material Processing and Manufacturing.

Xinjian Yuan graduated from Pusan National University of Korea in Department of Materials Science and Engineering and received a PhD in Materials Engineering in 2011. Presently, he is an associate professor in the College of Materials Science and Engineering, Chongqing University, China. His current research interests include welding and joining of metals and alloys.

Shiwei Tao is a M.Sc. candidate in the College of Materials Science and Engineering, Chongqing University. He is mainly engaged in TIG welding and joining of dissimilar aluminum alloy and titanium alloy.

Rui Li is a M.Sc. candidate in the College of Materials Science and Engineering, Chongqing University. He is mainly engaged in traditional welding and joining of dissimilar metals and electronic packaging.

Kanglong Wu graduated from Chongqing University in Department of Materials Science and Engineering and received a master's degree in Materials Engineering in 2019. His research interest is TIG welding and resistant spot welding of aluminum alloy and steel.